Geoscience Frontiers 14 (2023) 101629

Contents lists available at ScienceDirect

Geoscience Frontiers

journal homepage: www.elsevier.com/locate/gsf

Research Paper

Laser ablation (*in situ*) Lu-Hf dating of magmatic fluorite and hydrothermal fluorite-bearing veins

Stijn Glorie [a,*], Jacob Mulder [a], Martin Hand [a], Adrian Fabris [b], Alexander Simpson [a], Sarah Gilbert [c]

[a] Department of Earth Sciences, University of Adelaide, SA 5005, Australia
[b] Geological Survey of South Australia, Department for Energy and Mining, Adelaide, SA 5005, Australia
[c] Adelaide Microscopy, University of Adelaide, SA 5005, Australia

ARTICLE INFO

Article history:
Received 9 March 2023
Revised 25 April 2023
Accepted 19 May 2023
Available online 26 May 2023
Handling Editor: Krisotffer Szilas

Keywords:
Reaction-cell ICP-MS
In-situ geochronology
Fluorite-calcite veins
Iron oxide copper–gold
Critical mineral exploration
Rare Earth Elements

ABSTRACT

Fluorite (CaF_2) is a common hydrothermal mineral, which precipitates from fluorine-rich fluids with an exceptional capacity to transport metals and Rare Earth Elements (REEs). Hence, the ability to date fluorite has important implications for understanding the timing of metal transport in hydrothermal systems. Here we present, for the first time, fluorite Lu-Hf dates from fluorite-carbonate veins from the Olympic Cu-Au Province in South Australia. The fluorite dates were obtained *in situ* using the recently developed LA-ICP-MS/MS Lu-Hf dating method. A fluorite-calcite age of 1588 ± 19 Ma was obtained for the Torrens Dam prospect, consistent with the timing of the formation of the nearby Olympic Dam iron-oxide copper gold Breccia Complex. Veins in the overlying Neoproterozoic successions were dated at 502 ± 14 Ma, indicating a temporal link between Cu-sulphide remobilisation and the Delamerian Orogeny. Additionally, we present a multi-session reproducible date for magmatic fluorite from a monzogranite in the Pilbara Craton (Lu-Hf age of 2866 ± 19 Ma). This age is consistent with a garnet Lu-Hf age from the same sample (2850 ± 12 Ma) and holds potential to be developed into a secondary reference material for future fluorite Lu-Hf dating.

1. Introduction

Fluorite (CaF_2) is a common mineral in hydrothermal systems, where it precipitates from fluorine-rich fluids (Richardson and Holland, 1979). Such fluids have an exceptional capacity to carry metals, and are also thought to enhance mineralisation pathways by dissolving silicates along the fluid flow path (McPhie et al., 2011; Xing et al., 2019). Consequently, fluorite-bearing deposits can be extensive and are often carriers of elevated (economic) concentrations of critical commodities, such as Rare Earth Elements (REEs), particularly when associated with iron oxide-copper–gold (IOCG) systems (e.g. Williams-Jones et al., 2000; Schwinn and Markl, 2005; Williams et al., 2015). The supergiant Olympic Dam Fe-oxide Cu-U-Au-Ag deposit is a prominent example of an IOCG system and is hosted in a F-rich Mesoproterozoic silicic large igneous province (Allen et al., 2008; McPhie et al., 2011). Hence, fluorite is regarded as an important indicator mineral in IOCG (Schlegel et al., 2020) and other hydrothermal systems (Mao et al., 2015), such that understanding the timing of fluorite precipitation can provide critical information on the timing of metal transport and mineralisation.

Fluorite dating has previously been attempted by a variety of methods, including Sm-Nd (Chesley et al., 1991; Galindo et al., 1994), fission track (Groenlie et al., 1990), U-Th-Sm/He (Evans et al., 2005; Wolff et al., 2015; Wolff et al., 2016), and most recently, Pb-Pb and U-Pb (Piccione et al., 2019; Lenoir et al., 2021). However, all these methods have inherent challenges. Sm-Nd dates are derived from bulk dissolution and often produce isochrons that are compromised by incorporation of inclusions that are not in equilibrium with fluorite (e.g. Barker et al., 2009). Fission track and U-Th-Sm/He dating tends to produce low-temperature (~50–170 °C) cooling ages (Wolff et al., 2016) that are not necessarily related to the timing of fluorite precipitation. The novel fluorite Pb-Pb and U-Pb geochronometers have produced reliable dates (Piccione et al., 2019; Lenoir et al., 2021). However, they require sufficient U and low, but sufficiently variable, common-Pb for robust isochron regressions (cfr. Chew et al., 2014). Furthermore, little is known about Pb diffusion in fluorite, and post-mineralisation U-Pb fractionation has been documented (Bau et al., 2003), which indicates that the U-Pb and Pb-Pb systems in fluorite are unlikely

* Corresponding author.
E-mail address: stijn.glorie@adelaide.edu.au (S. Glorie).

https://doi.org/10.1016/j.gsf.2023.101629

to be robust, particularly when associated with complex IOCG mineralisation.

Here we present the first fluorite Lu-Hf dates, obtained from veins in both the late Paleoproterozoic basement and Neoproterozoic sedimentary cover sequences within the Olympic Cu-Au Province (e.g. Reid, 2019) in the eastern Gawler Craton (South Australia). We also present Lu-Hf dates from fluorite that crystallized in Mesoarchaean A-type granite from the Pilbara Craton, Western Australia (e.g. Huston et al., 2002; Roberts and Tikoff, 2021). This sample is largely used in this paper as a reference material for accuracy checks. The applied method is an *in situ* (laser ablation) approach, which was recently developed using a quadrupole mass-spectrometer, fitted with a reaction-cell, allowing ^{176}Lu and ^{176}Hf to be separated and measured free from isobaric interferences (Simpson et al., 2021). This method has been applied previously to date garnet (Brown et al., 2022; Tamblyn et al., 2022), apatite (Glorie et al., 2022; Glorie et al., 2023) and calcite (Simpson et al., 2022), but has not been applied to fluorite. Given that REEs in fluorite are thought to be generally resistant to volume diffusion (at temperatures < 500 °C; Cherniak et al., 2001), and that variations in initial Hf have negligible effects on Lu-Hf age calculations for radiogenic samples (Simpson et al., 2022; Glorie et al., 2023), this method overcomes some of the challenges presented above, and allows rapid and robust fluorite crystallization dates to be obtained in a variety of igneous and hydrothermal systems.

2. Geological background and sample descriptions

2.1. East Pilbara Terrane (Western Australia)

The East Pilbara Terrane is the Palaeoarchean core of the Pilbara Craton in western Australia (Van Kranendonk et al., 2007; Hickman and Van Kranendonk, 2012; Hickman, 2021). The terrane has a classic dome-and-keel architecture characterised by 50–100 km diameter felsic plutonic domes fringed by synclinal greenstone belts of the Pilbara Supergroup (Fig. 1). The Pilbara Supergroup includes voluminous ultramafic–mafic volcanic rocks and lesser felsic volcanic rocks, carbonate, chert, and siliciclastic strata that were deposited in several unconformity-bound cycles between ~ 3530 Ma and ~ 3235 Ma (Hickman and Van Kranendonk, 2012; Hickman, 2021). The domes are composite structures that comprise a series of plutonic supersuites that are time-equivalent to felsic volcanic cycles in the Pilbara Supergroup. With the exception of the oldest and least exposed Mulgundoona supersuite (~3530–3490 Ma), most plutonic supersuites are present in each of the nine domes exposed in the East Pilbara Terrane (Fig. 1; Hickman, 2021). The major dome-forming supersuites include the Callina (~3484–3462 Ma), Tambina (~3451–3416 Ma), Emu Pool (~3324–3290 Ma), Cleland (~3270–3223 Ma), and Sisters (~2954–2919 Ma) supersuites (Hickman, 2021). These supersuites document a progressive trend from early trondjemite-tonalite-granodiorite (TTG) suites to more evolved (monzogranitic) compositions with decreasing age (Champion and Smithies, 2007). The dome-forming supersuites record strong and polyphase deformation, which has been interpreted to reflect the episodic diapiric rise of the domes during partial convective overturn of the crust (Van Kranendonk, 2011; Wiemer et al., 2018; Roberts and Tikoff, 2021).

The stabilisation of the East Pilbara Terrane is marked by the emplacement of post-tectonic (unfoliated) granites of the ~ 2890–2880 Ma Cutinduna and ~ 2860–2830 Ma Split Rock supersuites (Van Kranendonk, 2011; Hickman and Van Kranendonk, 2012). These are the most evolved plutonic rocks in the East Pilbara Terrane and consist of moderately to highly fractionated two-mica monzogranites that are spatially and genetically associated with Li-Cs-Ta pegmatites (Sweetapple and Collins, 2002; Champion and Smithies, 2007). The timing of Split Rock Supersuite magmatism is not as well constrained as the other dome-forming supersuites (Hickman, 2021). Zircon U-Pb magmatic crystallization ages span ~ 2867–2831 Ma but are generally defined by a small number of grains (mostly < 5) and are compromised by Pb-loss, discordance, and inheritance (Nelson, 2004). In more detail, a sample of the Moolyella monzogranite in the Mount Edgar Dome was dated by U-Pb on zircon via SHRIMP with five analyses from the two youngest zircon grains yielding a weighted mean ^{207}Pb/^{206}Pb date of 2831 ± 11 Ma (95% confidence; Nelson, 2004). This sample also contains four older, near concordant (>90%) zircon grains, two of which yield a weighted mean ^{207}Pb/^{206}Pb date of 2862 ± 5 Ma (1σ). The Cookes Creek monzogranite (McPhee Dome) has also been dated by U-Pb on zircon via SHRIMP and yields a weighted mean ^{207}Pb/^{206}Pb date of 2837 ± 16 Ma (4 analyses on 3 grains; type of uncertainity not specified) for the youngest zircon population (Wingate et al., 2015). The youngest zircon population in the Bonny Downs monzogranite (Kurrana Terrane) yields a weighted mean ^{207}Pb/^{206}Pb date of 2838 ± 6 Ma (6 analyses on 3 grains dated via SHRIMP; 95% confidence) and also contains an older concordant zircon grain dated at 2861 ± 8 Ma (Nelson, 2005; Wingate et al., 2015). Magmatic zircon from the Spear Hill monzogranite in the Shaw Dome has a weighted mean ^{207}Pb/^{206}Pb date of 2851 ± 2 Ma (95% confidence) based on 18 analyses of 18 grains via SHRIMP (Nelson, 1998). Additional age constraints for the Split Rock Supersuite magmatism include a concordant U-Pb TIMS date of 2842.9 ± 0.3 Ma (type of uncertainity not specified) from placer monazite in a pegmatite field in the Mount Shaw Dome (Simonetti et al., 2006) and ~ 2890–2820 Ma ^{207}Pb/^{206}Pb dates from pegmatite-hosted cassiterite and columbite-group minerals from the Yule, Carlindi, and Mount Edgar domes obtained via SHRIMP (Kinny, 2000) and LA-ICP-MS (Kinny, 2000; Kendall-Langley et al., 2020).

Fluorite was sampled from an exposure of the Split Rock Supersuite (Moolyella Monzogranite) in the Mount Edgar Dome in the central parts of the East Pilbara Terrane (Fig. 1). The composite structure of the Mount Edgar Dome is defined by exposures of the oldest Callina and Tambina supersuite rocks along the southern and western margins, followed inward by volumetrically dominant rocks of the Emu Pool Supersuite, and a core of monzogranite plutons of the Cleland Supersuite (Fig. 1). The Moolyella Monzogranite comprises a massive, unfoliated, sub-horizontal sheet that intrudes banded orthogneiss of the ~ 3448–3416 Ma Fig Tree Gneiss (Tambina Supersuite) in the eastern parts of the dome (Hickman, 2021). The fluorite-bearing sample (EDG-1) was collected from the southeastern margin of the Moolyella Monzogranite, approximately 1 km southeast of a lithologically similar sample collected by the Geological Survey of Western Australia (GSWA 169044; Nelson, 2005). Sample EDG-1 is a massive, medium-grained, holocrystalline, two-mica monzogranite. Fluorite occurs as equant, <1 mm, purple-blue, generally inclusion-free grains intergrown with feldspar, quartz, and mica. The sample also contains minor garnet, which was dated by Lu-Hf in this study as an accuracy check for fluorite Lu-Hf dating.

2.2. Olympic Province (SA)

The Olympic Cu-Au Province (Skirrow et al., 2007) is located along the eastern margin of the Gawler Craton in South Australia (Fig. 2) and hosts a number of significant iron oxide-copper–gold (IOCG) deposits and prospects, including Olympic Dam, Carrapateena, and Prominent Hill (Reid, 2019). The basement is dominated by Palaeoproterozoic (~1.77 – 1.74 Ga) volcano-sedimentary sequences of the Wallaroo Group and granitic intrusions, which were variably affected by the ~ 1.74–1.69 Ga Kimban

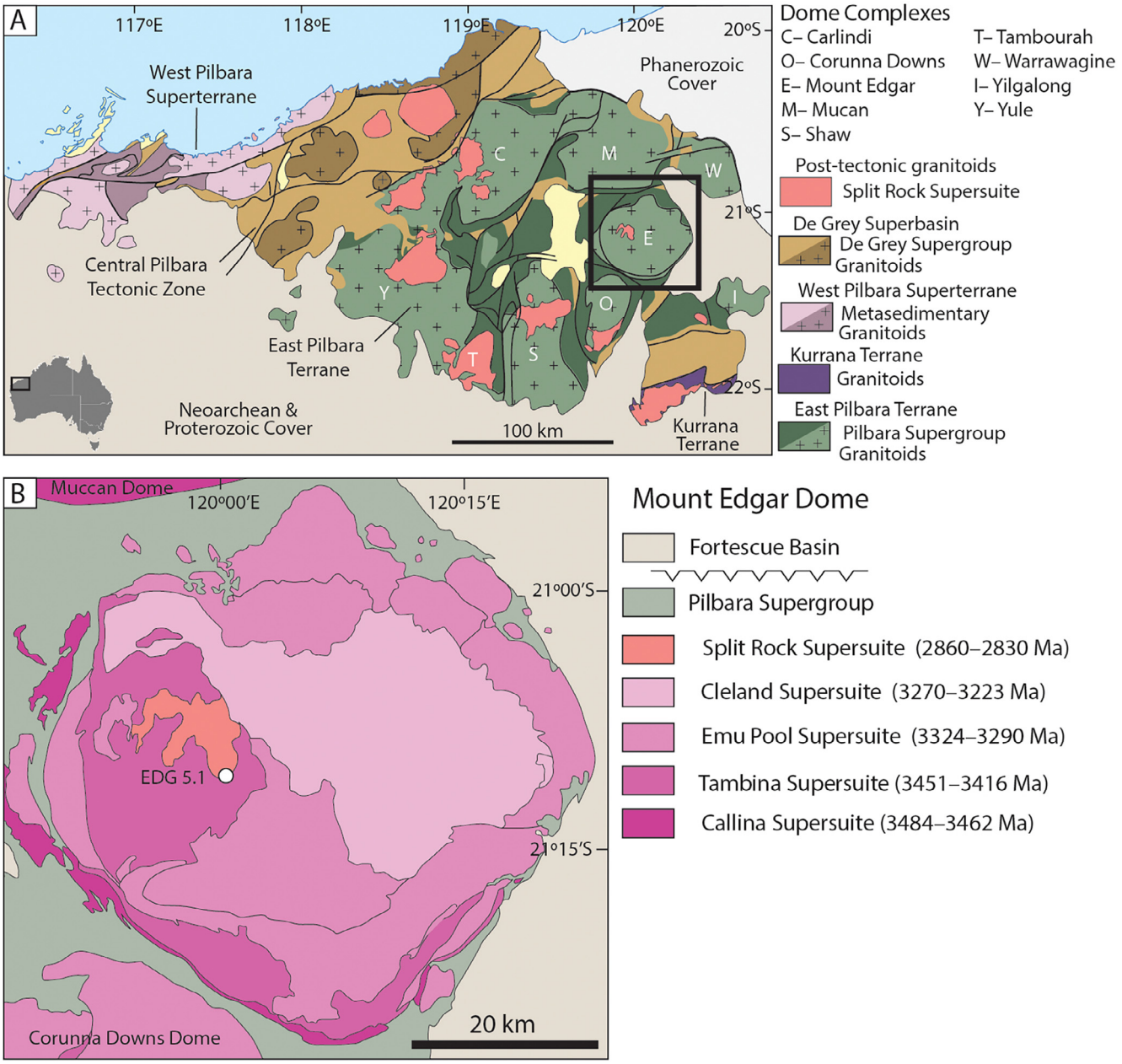

Fig. 1. Geological context of the Mount Edgar Dome, Pilbara Craton, Western Australia. (A) Major tectonic units of the northern Pilbara Craton highlighting granitic domes in the East Pilbara Terrane and the distribution of post-tectonic granitoids (modified from Hickman, 2021). (B) Simplified geological map of the Mount Edgar Dome showing the distribution of granitic supersuites and the location of fluorite-bearing sample EDG-1 (modified from Gardiner et al., 2017).

Orogeny (Hand et al., 2007; Szpunar et al., 2011). During the early Mesoproterozoic, the region was affected by extensive felsic-dominated magmatism expressed by the formation of the ~ 1595 – 1586 Ma Gawler Large Igneous Province (including the Hiltaba Suite and Gawler Range Volcanics) (e.g. Reid, 2019; Wade et al., 2022; Jagodzinski et al., 2023). The Olympic Dam Breccia Complex, which hosts the Olympic Dam deposits as well as the other major IOCG deposits, formed in the same time interval (e.g. Ehrig et al., 2021 and references therein). From the early Mesoproterozoic, red bed sandstones (Pandurra Formation) were deposited within a continental rift basin over large parts of the Olympic Cu-Au Province, although much of it has been removed through erosion. The mineralized basement system is also overlain by mid-to-late Neoproterozoic to Cambrian sequences (initiated at ~ 820 Ma) associated with the development of the Adelaide Superbasin (also known as the Adelaide Geosyncline and Adelaide Rift Complex) (e.g. Lloyd et al., 2020 and references therein). The flat-lying Neoproterozoic – Cambrian platform cover that overlies the eastern Gawler Craton (including the Olympic Cu-Au Province) is known as the Stuart Shelf, and is structurally separated from the main rift complex by the Torrens Hinge Zone (Fig. 2; Lambert et al., 1987; Reid, 2019). The Neoproterozoic sequences contain locally significant copper and associated cobalt mineralisation (Tonkin and Wallace, 2021). Cambrian sedimentation was terminated by the ~ 514 – 490 Ma Delamerian Orogeny (Foden et al., 2006; Foden et al., 2020). This resulted in the formation of a fold-and-thrust belt, magmatism, and locally high-temperature metamorphism in the bulk of the Adelaide Rift Complex, whereas the Stuart Shelf was largely unaffected (Reid and Fabris, 2015; Reid, 2019). Recent geochronology for the Olympic Dam deposit has revealed

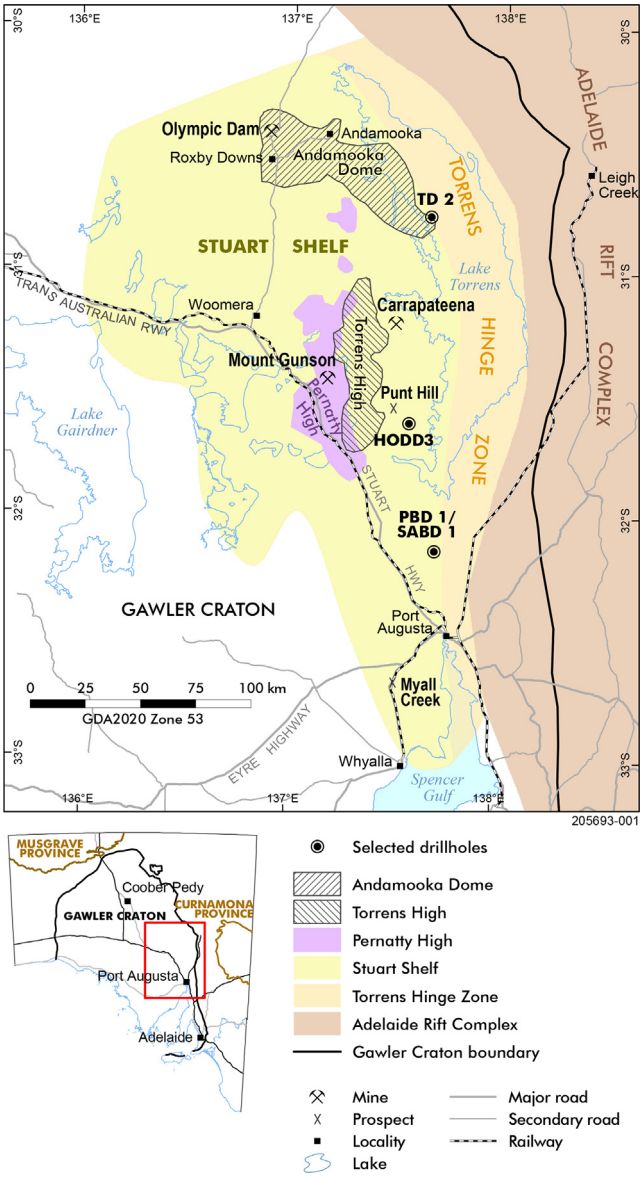

Fig. 2. Location map of the Stuart Shelf at the eastern margin of the Gawler Craton with indication of the major mineral deposits of the Olympic Cu-Au Province and the samples taken from basement rocks (drill hole TD-2) and Neoproterozoic sedimentary successions (drill holes HODD3 and PBD1/SABD1).

fluid flow that might have 'upgraded' the deposit either just prior to, or during the Delamerian Orogeny (Ehrig et al., 2021; Maas et al., 2022).

Fluorite (±calcite) veins occur in both the Olympic Cu-Au Province basement (Schlegel et al., 2020) and the overlying Neoproterozoic Stuart Shelf Cu deposits (Tonkin and Wallace, 2021). While they are often described as texturally 'late' features in the hydrothermal history of the IOCG deposits (e.g. Schmandt et al., 2017; Schlegel et al., 2018), little is known about their occurrence in the Stuart Shelf sequences. Given the common observation of Cu-sulphide minerals within the veins, and the common association of sulphide mineralisation with fluorite cements (Tonkin and Wallace, 2021), it is hypothesized that F-bearing fluids may have transported Cu from the Olympic Cu-Au Province basement into the overlying Neoproterozoic sequences. The Mount Gunson stratabound Cu-Co sulphide deposit on the Stuart Shelf (Fig. 2), which is hosted at the contact between the Mesoproterozoic Pandurra Formation and the Neoproterozoic Whyalla Sandstone, is an example of a significant Cu reserve that might have resulted from this process (Knutson et al., 1983).

Three samples were selected (Table 1) from drillcore stored at the South Australian Drill Core Reference Library. Sample TD-2 was taken from drill hole TD-2 (Fig. 2) from a coarse fluorite-carbonate vein cross-cutting K-feldspar-magnetite-chlorite ± hematite breccia of the Palaeoproterozoic (~1.75 Ga) Wandearah Formation (Fig. 3). Samples Tap-243 and Why-244 were taken from the Neoproterozoic Stuart Shelf successions (Fig. 2), from drill holes PBD1/SABD1 and HODD3, respectively. Sample Tap-243 is a fluorite vein in a brecciated interval of laminated siltstone of the Tapley Hill Formation (~643 Ma), and contains disseminated sulphides. Sample Why-244 represents a 4 mm wide fluorite-calcite vein that cross-cuts medium-grained Whyalla Sandstone (~643 Ma) (Fig. 3).

2.3. Analytical methods

Small (~1 cm) rock chips of the fluorite-bearing veins were cut out of drill core samples Tap-43, Why-44 and TD-2. For sample EDG-1, fluorite and garnet were liberated by crushing and conventional mineral separation, and mounted in epoxy resin disks. Following polishing, laser ablation (*in situ*) Lu-Hf dating was applied directly on the polished sections or separates. Analyses were conducted in 2 analytical sessions using a RESOlution-LR 193 nm excimer laser ablation system, coupled to an Agilent 8900 ICP-MS/MS. The laser beam diameter was set at 173 μm (EDG-1 fluorite) or 257 μm (all other fluorite-calcite samples) and ablation was conducted at 10 Hz repetition rate and a fluence of ~ 9 J/cm^2. See Supplementary Data File 1 for analytical conditions. The laser-based Lu-Hf method uses a NH_3 – He gas mixture in the reaction-cell of the mass spectrometer to promote high-order reaction products of Hf, with a mass-shift of + 82, while equivalent Lu and Yb reaction products are minimal (i.e. Hf reacts at a rate of 50%–60% while Lu reaction is < 0.003%; Simpson et al., 2021). Consequently, the resulting mass-shifted (+82 amu) reaction products of $^{176+82}$Hf and $^{178+82}$Hf can be measured free from isobaric interferences. ^{177}Hf was calculated from ^{178}Hf, assuming natural abundances. ^{175}Lu was measured on-mass as a proxy for ^{176}Lu (see details in Simpson et al., 2021, 2022). In addition to Lu and Hf isotopes, other trace elements, including a selection of other Rare Earth elements (REEs: Ce, Nd, Sm, Yb), were measured simultaneously to monitor for inclusions and to characterise the nature of the fluids. However, not every REE was measured as this would compromise the dwell times on the Hf isotopes required for age calculations.

Isotope ratios and trace element concentrations were calculated in LADR (Norris and Danyushevsky, 2018) using NIST 610 as a primary standard (Nebel et al., 2009). ^{43}Ca was used as internal standard element, assuming stoichiometric concentrations of 40.04 wt.% for calcite and 51.33 wt.% for fluorite. Reference calcite ME-1 (1530 ± 11 Ma; Duncan et al., 2011) was analysed repeatedly within each analytical session and used to correct the Lu-Hf isotope ratios for matrix-induced fractionation (Simpson et al., 2022). Given the similar ablation characteristics of fluorite and calcite under the applied analytical conditions (and the absence of Lu-Hf down-hole fractionation; Simpson et al., 2021), ME-1 was used as a calibration standard for both the calcite and fluorite Lu-Hf isotope ratios. Lu-Hf ages were calculated as inverse isochrons using IsoplotR (Vermeesch, 2018; Li and Vermeesch, 2021). For samples that produced exclusively high-radiogenic ^{177}Hf/^{176}Hf ratios (< ~0.1), the isochron was anchored to an initial ^{177}Hf/^{176}Hf composition of 3.55 ± 0.05, which spans the entire range of initial ^{177}Hf/^{176}Hf ratios of the terrestrial reservoir (e.g. Spencer et al., 2020). Additionally, a weighted mean Lu-Hf date was calculated in IsoplotR, directly from the (matrix-corrected) ^{176}Hf-^{176}Lu ratios for

Table 1
Sample details.

Sample name	Sample n°	Drill hole	Latitude (°N)	Longitude (°E)	Depth	Stratigraphy	Description
Edgar Dome, Pilbara (WA)							
EDG-1	EDG 5.2	NA (outcrop)	−21.17712	120.00303	outcrop	*Split Rock Supersuite*	Fluorite in granite
Stuart Shelf (SA)							
Tap-243	R4220243	SABD1 (147219)	−32.1519334	137.7024455	622 m	*Tapley Hill Fm.*	Fluorite vein in a brecciated interval within laminated siltstone, which also contains disseminated sulphides
Why-244	R4220244	HODD3 (268313)	−31.6301654	137.5676596	332 m	*Whyalla Sandstone*	4 mm wide fluorite-calcite vein that cross-cuts medium-grained sandstone
TD-2	R4225960	TD2 (25384)	−30.7803904	137.6526246	857 m	*Wallaroo Group (Wandearah Fm.)*	Very coarse carbonate - fluorite vein cross-cutting haematite-magnetite-chlorite breccia

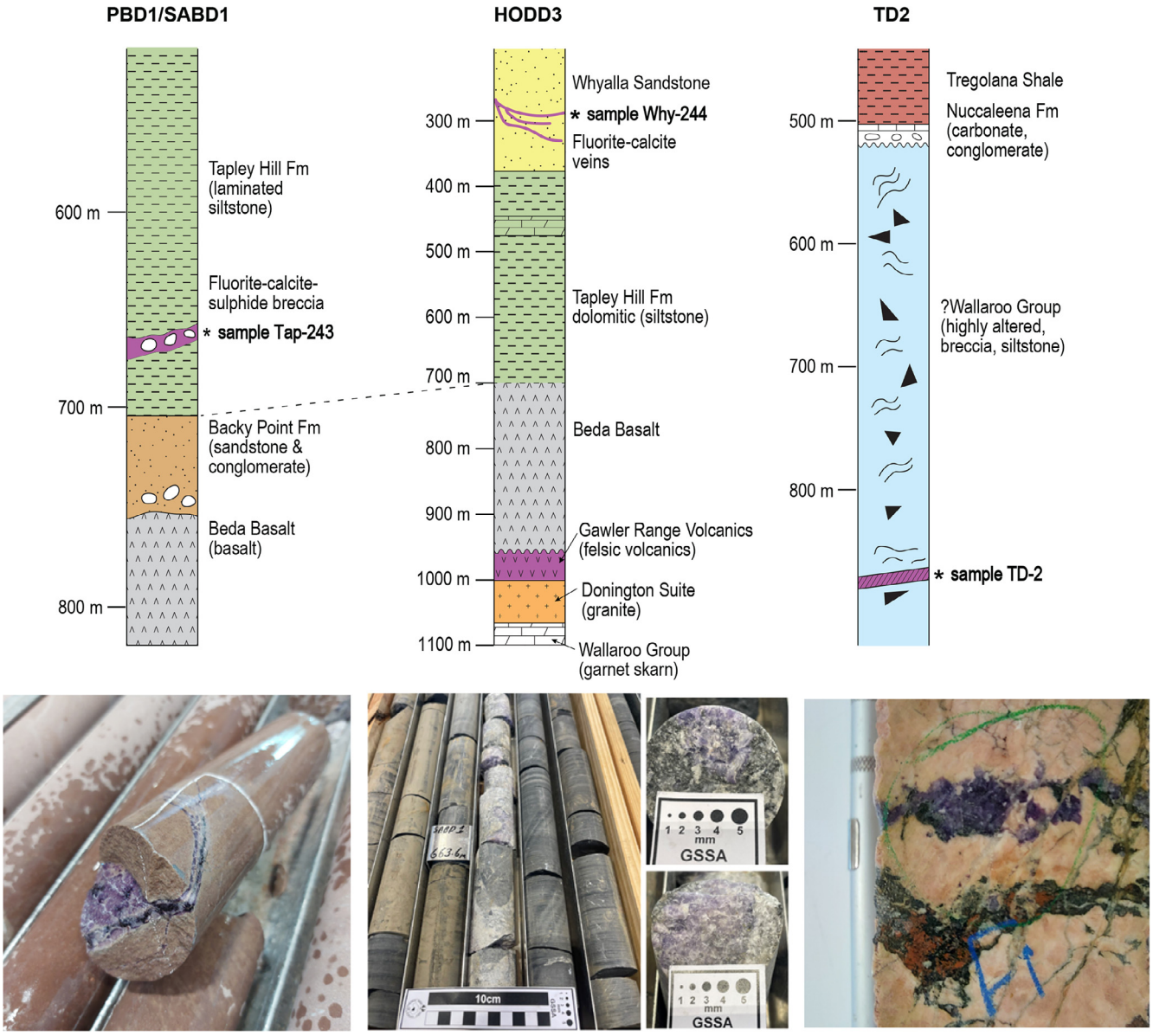

Fig. 3. Drill core stratigraphy and fluorite pictures for the Stuart Shelf study area.

such highly radiogenic ($^{177}Hf/^{176}Hf$ ratios < 0.1) data. No common Hf corrections were applied as they have negligible effects to the calculated ages (Simpson et al., 2022; Glorie et al., 2023). The in-house reference calcite MKED (expected Lu-Hf age: 1517.3 ± 0.3 Ma; measured age: session 1 = 1516 ± 29 Ma; session 2 = 1517 ± 22 Ma) was monitored for accuracy checks and is in

excellent agreement with previously published data (Table 2; Supplementary Data File 2; Simpson et al., 2022). EDG-1 fluorite was measured in both analytical sessions and serves as an accuracy check for the fluorite Lu-Hf dates in this paper. Additionally, garnets from sample EDG-1 were analysed for Lu-Hf isotopes to have an independent Lu-Hf reference age from the same sample. The applied analytical method for garnet Lu-Hf dating is identical to the fluorite/calcite method with the exception that a smaller laser beam diameter of 100 μm and lower laser fluency of ~ 3 J/cm^2 were used. The Hogsbo garnet reference material was used as matrix-matched calibration standard (Simpson et al., 2021) and BP-1 reference garnet (measured age = 1744 ± 13 Ma; expected reference age = 1745 ± 14 Ma; Simpson et al., 2023) was used as an accuracy check (Supplementary Data File 3). For all analysed samples (fluorite, calcite, and garnet), the reported uncertainties for the inverse isochron and weighted mean Lu-Hf dates are presented as 95% confidence intervals and include the propagated uncertainties from the matrix-matched calibration standards.

3. Results

The REE trace element compositions are summarised on a chondrite-normalised Ce/Yb versus Ce/Sm biplot in Fig. 4. Associated chondrite-normalised spidergraphs (plotted with GCDKit; Janousek et al., 2006) can be found in Supplementary Data File 4.

Table 2 provides a summary of the calculated ages for all samples and reference materials. The associated data spreadsheet is provided as Supplementary Data File 5 and inverse isochron and weighted mean age plots are presented in Figs. 5, 6 and 7.

3.1. Sample EDG-1 (Edgar Dome granite, WA)

Based on the trace-element composition, the fluorite in sample EDG-1 can be subdivided into a relatively REE-rich and REE-poor population. The REE-rich population has elevated LREE concentrations (~600 – 2000 ppm Ce), with Lu concentrations ranging between ~ 6 and 16 ppm (Supplementary Data File 5) and chondrite-normalised Ce/Yb ratios > 1 (Fig. 4). The REE-poor population has < 6 ppm Ce and Lu and, consequently, shows comparatively flat to positively sloping chondrite-normalised REE trends (Ce/Yb ratios < 1; Fig. 4; Supplementary Data File 4). The REE-rich population is characterized by highly radiogenic Lu-Hf compositions, with $^{177}Hf/^{176}Hf$ ratios generally < 0.2. The REE-poor fluorite produces highly variable $^{177}Hf/^{176}Hf$ ratios, ranging between ~ 0.2 and 3.6. Consequently, single-spot fluorite Lu-Hf dates can be calculated for the REE-rich population, while the

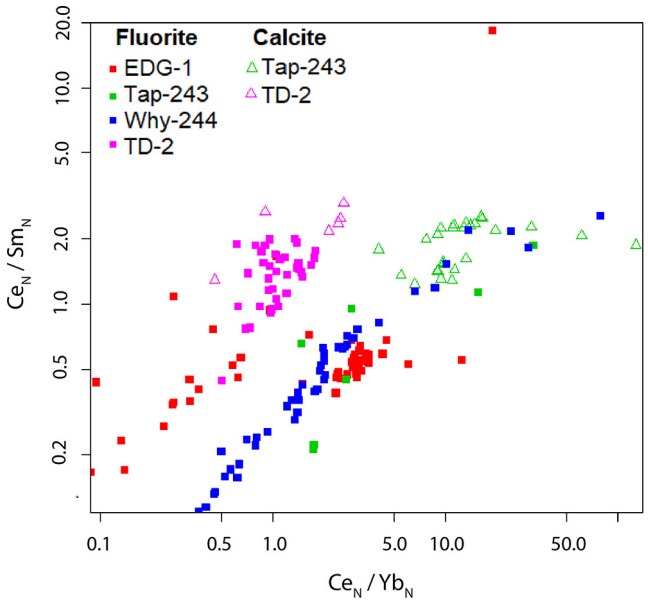

Fig. 4. Ce/Yb ratio versus Ce/Sm ratio (both normalized to chondrite) biplot for the studied fluorite (filled symbols) and calcite (open symbols) samples, summarizing the Rare Earth Element trends in the trace element data.

REE-poor population requires an isochron regression to calculate a fluorite Lu-Hf date. However, the REE-rich and REE-poor fluorites produce consistent ages when comparing the single-spot weighted mean Lu-Hf and isochron dates (Fig. 5). For analytical session 1, an inverse isochron date of 2865 ± 23 Ma was obtained (34 analyses, MSWD = 0.88), while the weighted-mean single-spot Lu-Hf age was calculated as 2869 ± 27 Ma (14 analyses, MSWD = 0.46). For analytical session 2, the inverse isochron and single-spot Lu-Hf dates were calculated as 2868 ± 20 Ma (18 analyses, MSWD = 0.88) and 2875 ± 23 Ma (7 analyses; MSWD = 0.46), respectively. Hence, the dates for the two analytical sessions are in excellent agreement, within uncertainty, and a combined inverse isochron fluorite Lu-Hf date was calculated as 2866 ± 19 Ma (52 analyses, MSWD = 0.83). The combined single-spot Lu-Hf dates produced a weighted mean date of 2872 ± 21 Ma (Table 2; Fig. 5).

3.2. TD-2 fluorite-calcite vein (Wallaroo Group, Torrens Dam prospect, SA)

Both fluorite and calcite were analysed from a single vein within the Torrens Dam drillcore (TD-2). The REE concentrations are

Table 2
Summary of obtained Lu-Hf ages. Iso Age = inverse isochron age and WM Age = weighted mean age. MSWD = mean squared weighted deviation; *n* = number of analyses; s1 = analytical session 1, s2 = analytical session 2, comb = ages for combined sessions.

Sample	Iso Age (Ma)	2σ (Ma)	MSWD (*n*)	WM Age (Ma)	2σ (Ma)	MSWD (*n*)
Calcite						
MKED s1	1517	24	1.5 (13)	1516	30	0.7 (13)
MKED s2	1520	23	1.9 (24)	1517	22	1.8 (24)
MKED comb	1519	18	1.7 (37)	1517	15	1.4 (37)
Tap-243	503	15	0.6 (26)	505	15	0.8 (23)
TD-2	1587	33	0.2 (6)	1590	39	0.2 (6)
Fluorite						
EDG-1 s1	2865	13	0.9 (34)	2869	19	0.5 (14)
EDG-1 s2	2871	14	0.9 (18)	2875	18	0.5 (7)
EDG-1 comb	2867	10	0.9 (52)	2872	13	0.5 (21)
Why-244	500	53	0.8 (45)	-	-	-
Tap-243	471	86	0.5 (7)	-	-	-
TD-2	1588	21	1.3 (35)	-	-	-
Combined						
Tap-243+Why-244	502	14	0.7 (78)			
TD-2	1588	18	1.1 (41)			

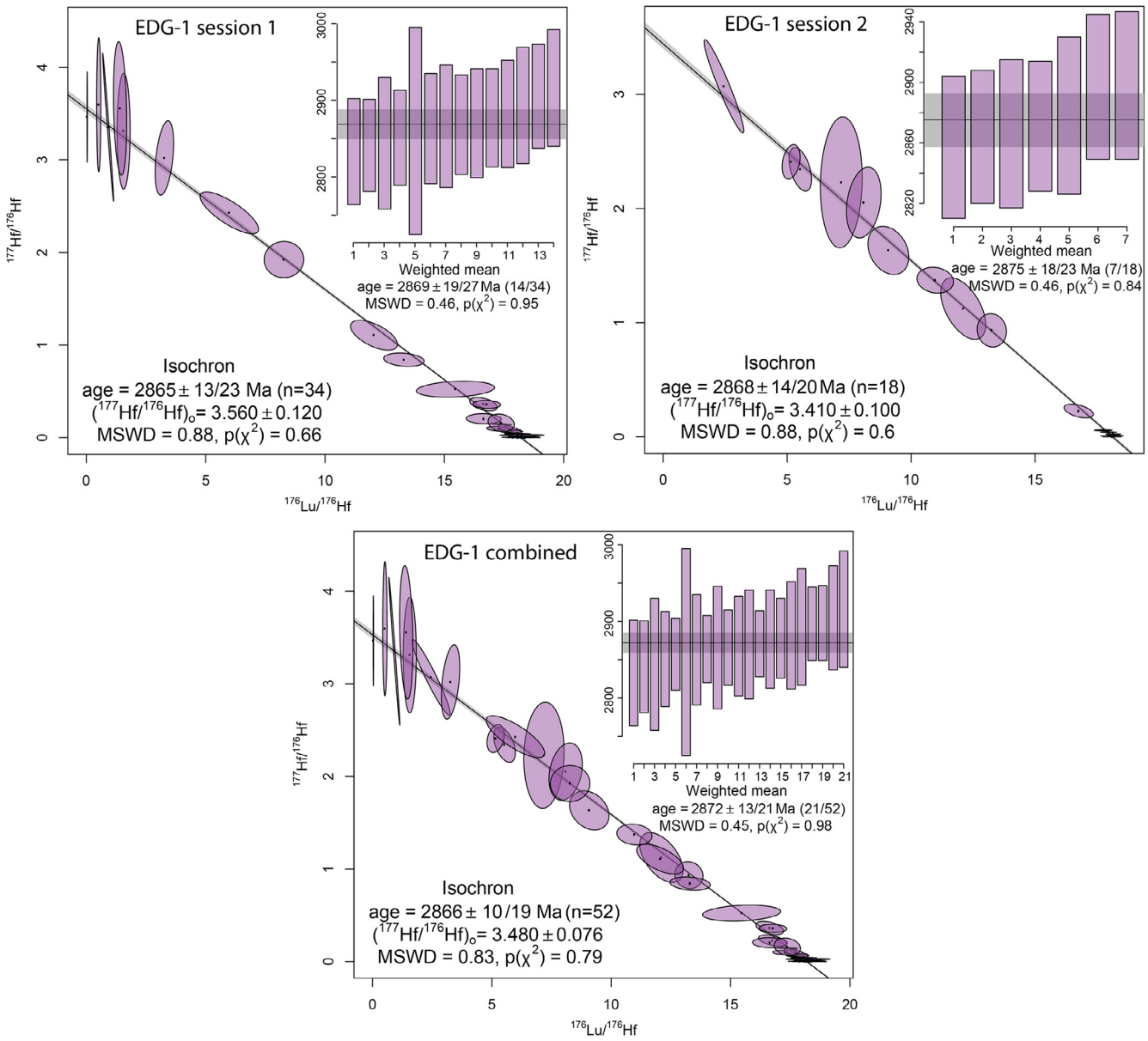

Fig. 5. Lu-Hf inverse isochron and weighted mean plots for the EDG-1 fluorite sample form the East Pilbara Terrane. The top panels present the results from two analytical sessions individually, and the bottom plot combines all analytical data in a single inverse isochron and weighted mean plot. For each sample, two uncertainties are reported. The first number is the 95% confidence uncertainty, and the second number includes the propagated uncertainty from the calibration standard.

similar in both minerals, with relatively flat chondrite-normalized REE trends and associated normalised Ce/Yb and Ce/Sm ratios of ~ 1–3 (Fig. 4; Supplementary Data File 4) and Lu concentrations ranging between ~ 0.1 ppm and 3.7 ppm (Supplementary Data File 5). The calcite analyses, however, are much more radiogenic with $^{177}Hf/^{176}Hf$ ratios < 0.1, regardless of the Lu concentration. For the fluorite, the $^{177}Hf/^{176}Hf$ ratios range between ~ 0.3 and ~ 3.3, which is an excellent isotopic variability for a robust isochron regression. The calculated fluorite inverse isochron date for sample TD-2 is 1588 ± 22 Ma (36 analyses, MSWD = 1.3; Fig. 6). For the calcite, an anchored inverse isochron date of 1587 ± 34 Ma (6 analyses, MSWD = 0.21) and weighted-mean single-spot date of 1590 ± 40 Ma (6 analyses, MSWD = 0.24) were obtained. Hence, the calcite and fluorite Lu-Hf dates are in excellent agreement and a combined Lu-Hf inverse isochorn age of 1588 ± 19 Ma (42 analyses, MSWD = 1.1) was calculated for the TD-2 fluorite-calcite vein sample (Table 2; Fig. 6).

3.3. Vein samples Tap-243 and Why-244 (Tapley Hill and Whyalla Formation, SA)

Similar to sample TD-2, sample Tap-243 contains calcite and fluorite in a single vein. The calcite in the Tap-243 vein is strongly enriched in REEs compared to the fluorite (the average Ce and Lu concentrations are respectively > 30 × and > 20 × higher in the calcite) and both minerals display negatively sloping chondrite normalized REE trends and relatively high Ce/Yb ratios (Fig. 4; Supplementary Data File 4). The Lu concentration is ~ 0.6 – 1.2 ppm for the calcite and ~ 0.03 – 0.07 ppm for the fluorite (Supplementary Data File 5). The calcite has highly radiogenic $^{177}Hf/^{176}Hf$ ratios (23/26 analyses < 0.1), while the fluorite has more initial Hf ($^{177}Hf/^{176}Hf$ ratios of ~ 1.1 – 2.4). Consequently, the uncertainty on the fluorite Lu-Hf date is large (471 ± 85 Ma; Fig. 7), illustrating a limitation of the method for Lu-poor fluorite samples. The calcite Lu-Hf data produces a more precise anchored

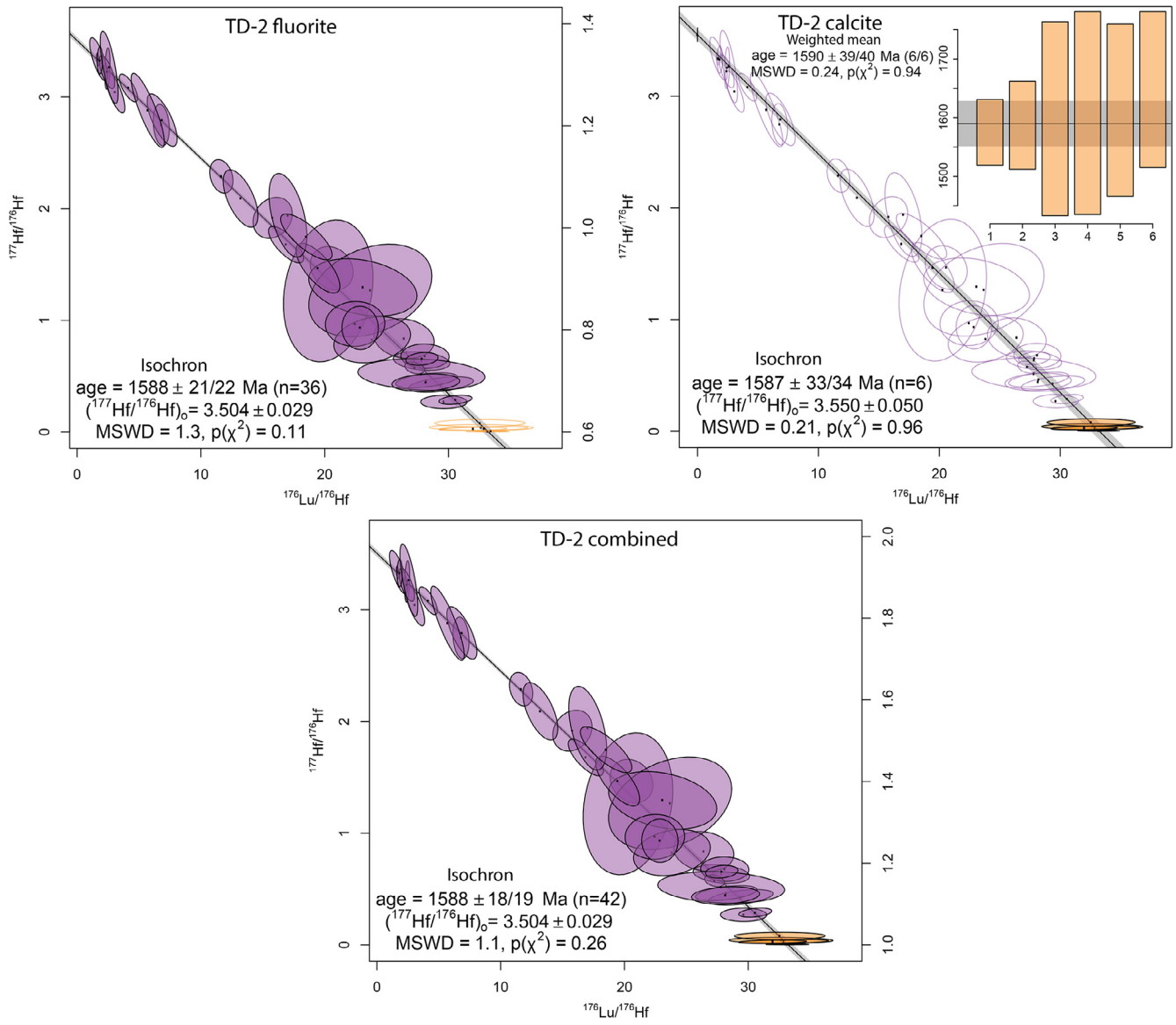

Fig. 6. Lu-Hf inverse isochron and weighted mean plots for the TD-2 sample from the Torrens Dam (TD-2) drill hole. Fluorite data is indicated by purple ellipses and calcite is shown by orange ellipses and error bars in the weighted mean plot. In the top left panel, the calcite data is not included in the isochron regression and presents the obtained Lu-Hf age for fluorite only. In the top right panel, age calculations are based on calcite only. The bottom panel combines both the calcite and fluorite data in an inverse single isochron. For each sample, two uncertainties are reported. The first number is the 95% confidence uncertainty, and the second number includes the propagated uncertainty from the calibration standard. (For interpretation of the references to colour in this figure legend, the reader is referred to the web version of this article.)

inverse isochron date of 503 ± 14 Ma (26 analyses, MSWD = 0.61) and a weighted mean single-spot date of 505 ± 16 Ma (23 analyses with $^{177}Hf/^{176}Hf$ ratios < 0.1; MSWD = 0.76) (Table 2; Fig. 7).

In contrast to sample Tap-243, there is no calcite associated with the Why-244 fluorite vein. The Chondrite-normalised REEs reveal a strong positive correlation between Ce/Sm and Ce/Yb ratios in fluorite (Fig. 4), with most data showing low LREE compared to MREE concentrations (expressed as Ce/Sm ratios < 1) (Supplementary Data File 4). Lu concentrations range between ~ 0.14 ppm and ~ 0.45 ppm and $^{177}Hf/^{176}Hf$ ratios are highly variable, ranging from ~ 3.6 to ~ 1.5. Analyses with higher (less radiogenic) $^{177}Hf/^{176}Hf$ ratios have elevated Zr concentrations (Supplementary Data File 5), indicating that these data may be affected by the presence of zircon micro-inclusions. The Lu-Hf ratios plot on a single inverse isochron, from which a fluorite Lu-Hf date of 497 ± 53 Ma (45 analyses, MSWD = 0.76) was calculated (Table 2; Fig. 7).

In order to demonstrate the time equivalence of the two analysed fluorite veins in the Tapley Hill and Whyalla Formations, the data was pooled in a single inverse isochron plot, producing an under dispersed Lu-Hf date of 502 ± 14 Ma (78 analyses, MSWD = 0.67; Fig. 7).

4. Discussion

4.1. Fluorite REE compositions

In order to evaluate the fluid-types from which the fluorite crystallized, a modified version of the fluorite REE classification plot of Möller et al. (1976) and Schlegel et al. (2020) was calculated. Given that we did not analyse La and Tb, our modified diagram uses Sm/Ce and Sm/Ca ratios in favour of Tb/La and Tb/Ca ratios, respectively. Published data from Prominent Hill and Olympic Dam fluorite demonstrate a linear correlation between the traditional and

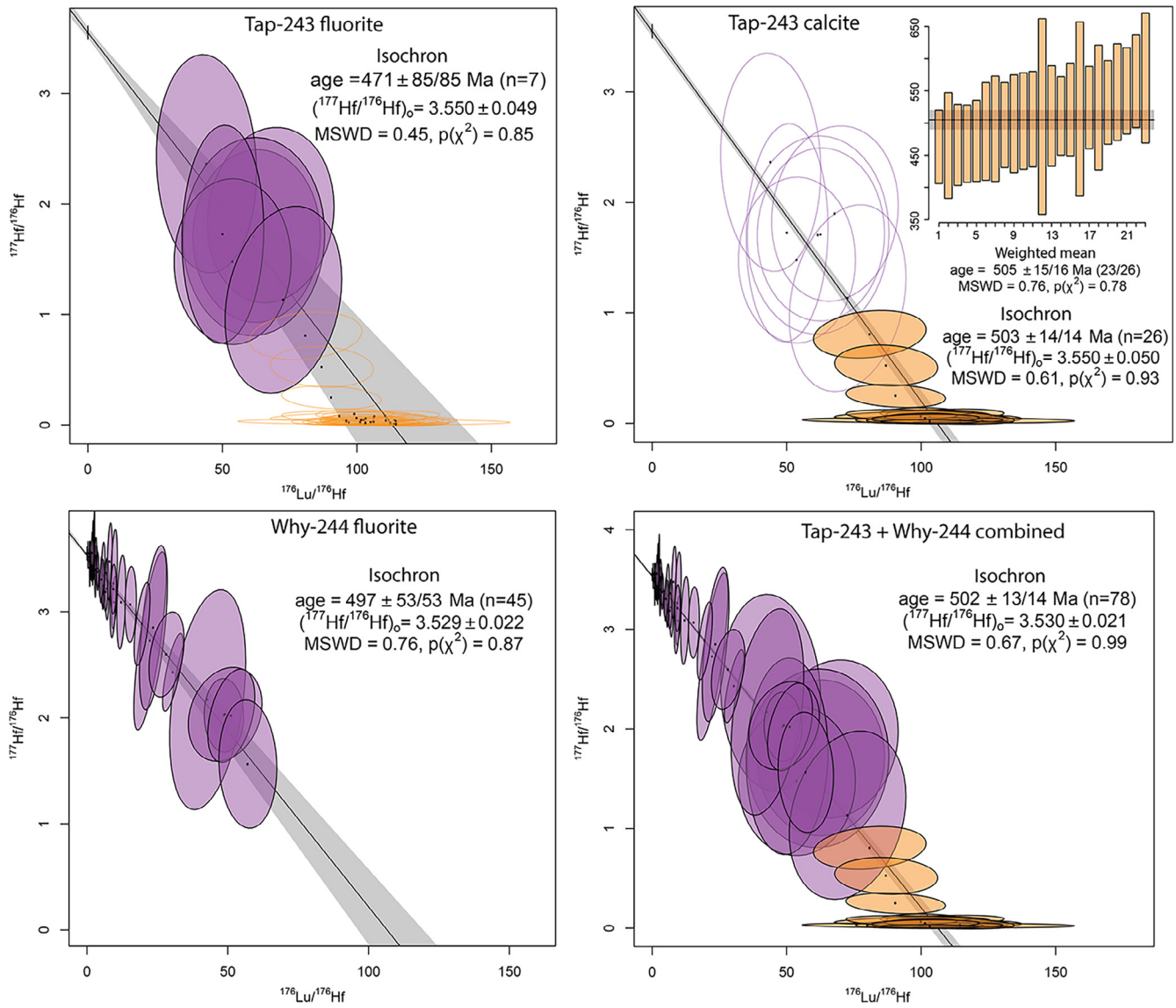

Fig. 7. Lu-Hf inverse isochron and weighted mean plots for the Tap-243 (top panels) and Why-244 (bottom left) samples. Fluorite data is indicated by purple ellipses and calcite is shown by orange ellipses and error bars in the weighted mean plot. In the top left panel, the calcite data is not included in the inverse isochron regression and presents the obtained Lu-Hf age for fluorite only. In the top right panel, age calculations are based on calcite only. For the Why-244 sample, only fluorite Lu-Hf ages were obtained. The bottom right panel combines all analysed data for both fluorite and calcite for both samples. For each sample, two uncertainties are reported. The first number is the 95% confidence uncertainty, and the second number includes the propagated uncertainty from the calibration standard. (For interpretation of the references to colour in this figure legend, the reader is referred to the web version of this article.)

revised ratios (Supplementary Data File 6). The resulting diagram (Fig. 8) shows that the main fluorite population from sample EDG-1 (fluorite in monzogranite) plots in the epithermal (pegmatitic) field. This is consistent with the interpretation that the fluorite formed late in the magmatic crystallisation. The Stuart Shelf vein samples plot largely in the magmatic-hydrothermal field in a similar area as the magmatic fluorite veins from Prominent Hill. The REE data for the fluorite vein in the Whyalla Formation, however, defines a broadly linear trend that crosses from the magmatic-hydrothermal field towards the sedimentary field. This trend-line mimicks the shape of a remobilisation trend, where LREEs are sequentially depleted with respect to MREEs, while the Sm/Ca ratio remains unaffected (Möller et al., 1976). Hence, the fluorite trace element data reveals that REEs were remobilised from their magmatic source towards the Neoproterozoic Tapley Hill and Whyalla sedimentary sequences. This trend further indicates that care needs to be exercised when interpreting fluorite trace element data in the context of fluid sources because there is no evidence of Cambrian magmatism in the eastern Gawler Craton (e.g. Reid, 2019). Instead, it appears fluorite may be able to record compositions that mimick the origin of source rocks that are unrelated to those the fluids interacted with.

4.2. A precise archaean Lu-Hf date for magmatic fluorite in the Pilbara

The fluorite Lu-Hf isochron age of 2866 ± 19 Ma for EDG-1 is in good agreement with the obtained garnet Lu-Hf age for the same sample (2850 ± 12 Ma). This agreement gives confidence that the use of a calcite calibration standard is likely appropriate to correct fluorite Lu-Hf ratios for laser-induced fractionation. Additional laser-induced fractionation between calcite and fluorite is thus insignificant within the achievable precision of the applied method. Both Lu-Hf dates broadly overlap, within uncertainty, with the published interpreted magmatic zircon age for the Moolyella

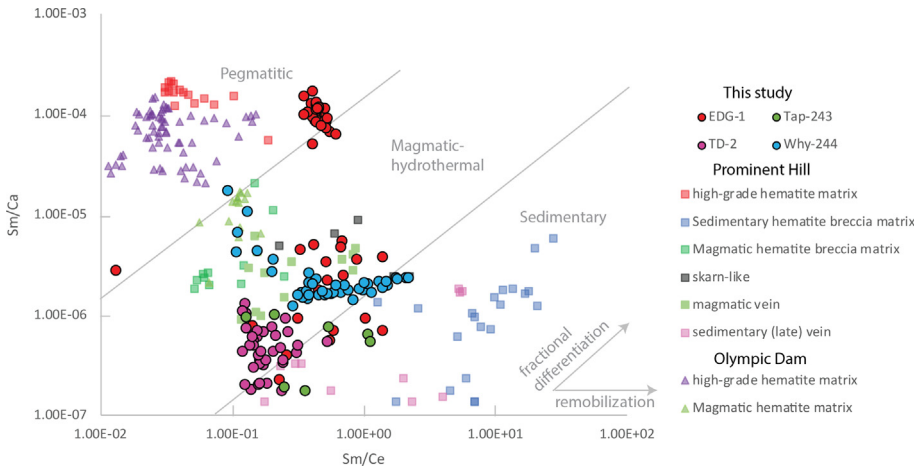

Fig. 8. Modified version of the fluorite REE classification plot of Möller et al. (1976) and Schlegel et al. (2020) using Sm/Ca versus Sm/Ce ratios instead of Tb/La versus Tb/Ca ratios. La and Tb were not analysed in our analytical sessions and we recalculated the published Tb/La and Tb/Ca ratios for fluorites from Prominent Hill and Olympic Dam to Sm/Ce and Sm/Ca ratios, which are lineary correlated when plotted as logarithmic values (Supplementary Data File 5).

Monzogranite of 2831 ± 11 Ma (sample GSWA 169044, Nelson, 2005) and U-Pb cassiterite ages of 2839 ± 16 Ma (Kinny, 2000) and 2843 ± 9 Ma (Kendall-Langley et al., 2020) from genetically associated pegmatites. As with most plutons of the Split Rock Supersuite, the age of the Moolyella Monzogranite is poorly constrained (see section 2.1). The 2831 ± 11 Ma preferred magmatic age of GSWA 169044 is based on 5 analyses of 2 zircon grains (Nelson, 2005). However, this sample also contains 4 grains that yield older ages of 2861 Ma, 2863 Ma, 2887 Ma, and 2905 Ma, with the two most concordant of these grains yielding a weighted mean age of 2862 ± 5 Ma (1σ). Nelson (2005) suggested these 4 older grains were xenocrysts but this interpretation is difficult to reconcile with the lack of intrusions younger than the Cleland Supersuite (3270–3223 Ma) in the Mount Edgar Dome (Fig. 1). Similar zircon U-Pb age complexities are observed in other dated plutons of the Split Rock Supersuite (see section 2.1). Sample GSWA 142879 (Shaw Dome) has a preferred magmatic age of 2851 ± 2 Ma but also includes a 100% concordant zircon grain dated at 2867 ± 5 Ma (1σ) (Nelson, 1998). Similarly, sample GSWA 178014 (Kurrana Terrane) has a preferred magmatic age of 2861 ± 4 Ma (1σ) based on a single zircon grain but also contains a younger zircon age population (n = 3) at 2838 ± 12 Ma (Nelson, 2005).

More work is needed to refine the magmatic age of the Moolyella Monzogranite, and the Split Rock Supersuite. However, the obtained Lu-Hf ages of 2850 ± 12 Ma (garnet) and 2866 ± 19 Ma (fluorite) from the same sample (EDG-1) are consistent with the 2862 ± 5 Ma zircon population in GSWA 169044 and may indicate prolonged emplacement of the Moolyella Monzogranite between ca. 2860 Ma and ca. 2830 Ma. This interpretation is consistent with the findings of Hickman (2021), who noted that although the Split Rock Supersuite magmatism is generally considered to have occurred at 2851–2831 Ma, there is evidence that some post-orogenic granitoids in the Pilbara Craton nominally assigned to this supersuite were emplaced as early as ~ 2880 Ma.

4.3. Two episodes of fluorite veins in the Stuart Shelf

4.3.1. ~ 1590 Ma fluorite in the Olympic Cu-Au Province

A fluorite-carbonate vein (sample TD-2) cross-cutting hematite-magnetite-chlorite breccia at the Torrens Dam prospect (Olympic Cu-Au Province, South Australia) gives an age of 1588 ± 19 Ma. This age is consistent with the ~ 1595 – 1575 Ma timing of IOCG development in the Olympic Cu-Au Province (e.g. Reid, 2019), including the ~ 1590 Ma Olympic Dam Breccia Complex (e.g. Johnson and Cross, 1995), which hosts the supergiant Olympic Dam Fe-oxide Cu-U-Au-Ag deposit. Geochronological constraints on the Olympic Dam Breccia Complex are extensive. The host Roxby Downs Granite crystallised at 1593.3 ± 0.3 Ma (Courtney-Davies et al., 2020), and the hydrothermal system was active after 1591.0 ± 0.6 Ma (Cherry et al., 2018). Additionally, hydrothermal U-rich hematite formed at 1592 ± 15 Ma, 1590 ± 8 Ma, and 1577 ± 5 Ma, fluorapatite at 1583 ± 7 Ma and uraninite at 1594 ± 5 Ma and 1588 ± 4 Ma (Ciobanu et al., 2013; Apukhtina et al., 2017; Ehrig et al., 2021). To the south of the Torrens Dam Prospect, Re-Os dating of pyrite in the Carrapateena IOCG deposit gives a 1598 ± 6 Ma date (Sawyer et al., 2017). Hence, the Torrens Dam fluorite ages are in excellent agreement with previous geochronological constraints for the Olympic Dam and Carrapateena IOCG deposits, demonstrating a temporal link between fluorite veining in Torrens Dam and hydrothermal activity resulting in world class mineralisation.

4.3.2. IOCG remobilisation in Delamerian fluorine-rich fluids

The fluorite-bearing veins in the Tapley Hill Formation (Tap-243) and Whyalla Sandstone (Why-244) yield consistent Lu-Hf dates that together indicate widespread hydrothermal activity on the Stuart Shelf. These dates are significantly younger than the Sturtian depositional age of the sediments (643 ± 2 Ma Re-Os age for the base of the Tapley Hill Formation; Kendall et al., 2006). Although the closure temperature of Lu diffusion in fluorite is not well constrained, theoretical calculations suggest that REEs in fluorite are largely immobile at < 500 °C on a scale smaller than the employed laser beam diameter (Cherniak et al., 2001). Given that the veins occur in sedimentary rocks that have only experienced diagnesis (Preiss, 1987; Tonkin and Wallace, 2021), the fluorite-calcite Lu-Hf dates are interpreted as primary precipitation ages. The ~ 502 Ma fluorite-calcite Lu-Hf ages are consistent with the timing of the Delamerian Orogeny, and more specifically, with the mid- to late Cambrian stage of back-arc extension and associated deformation and magmatism in eastern South Australia (Foden et al., 2006; Foden et al., 2020).

Hydrothermal activity at ~ 0.5 Ga has previously been identified in the eastern Gawler Craton. Ehrig et al. (2021) presented uraninite U-Pb ages of 532 ± 7 Ma and 474 ± 5 Ma for the Olympic Dam Breccia Complex, revealing a staged evolution for uranium mineralisation within the Olympic Dam deposit, which was likely upgraded by tectonically induced Ediacaran-Cambrian fluid flow. Maas et al. (2022) obtained ~ 0.5 Ga carbonate Sm-Nd ages (including from fluorite-barite-bearing veins) and associated Sr iso-

topic ratios that support a multi-stage evolution of the Olympic Dam deposit, with evidence for Cu-sulphide formation during the Delamerian Orogeny. This conforms with our interpretations that the Delamerian Orogeny induced fluid flow and fluorite precipitation in cover sediments overlying the Olympic Cu-Au Province. The analysed veins in the Tapley Hill Formation and Whyalla Sandstone contain sulphide inclusions, including chalcopyrite (e.g. Tonkin and Wallace, 2021), indicating the causative fluids mobilized metals. While speculative at this stage, the evidence for ~ 500 Ma fluid-rock interaction within the Olympic Dam deposit (Ehrig et al., 2021; Maas et al., 2022) suggests Cu mineralisation within the Stuart Shelf Neoproterozoic units could have been sourced from the underlying early Mesoproterozoic IOCG deposits. Given the exceptional capacity of fluorine to transport metals (McPhie et al., 2011; Xing et al., 2019), the interpretation of metal and REE remobilisation during the Delamerian Orogeny might present significant opportunities for stratabound mineral exploration in the Stuart Shelf and associated Adelaide Superbasin, given the presence of world class Cu deposits in the underlying basement.

5. Conclusions

(1) This work produced the first Lu-Hf dates for fluorite and demonstrates that accurate and precise results can be obtained with LA-ICP-MS/MS instrumentation. For fluorite-carbonate veins, both mineral phases should be analysed for increased precision.
(2) An isochronically homogenous fluorite separate from a monzogranite in the Pilbara Craton (EDG-1) was identified as a potentially suitable (secondary) reference material for future fluorite Lu-Hf dating. The multi-session fluorite Lu-Hf age of 2866 ± 19 Ma is in agreement with a garnet Lu-Hf age for the same sample (2850 ± 12 Ma) and with published zircon U-Pb ages for nearby locations.
(3) A fluorite-calcite vein in drillcore from Torrens Dam within the Olympic Province was dated at 1588 ± 19 Ma, which is in excellent agreement with the timing of the formation of the Olympic Dam Breccia Complex. Hence, fluorite Lu-Hf may be a suitable method to directly date hydrothermal alteration and IOCG genesis.
(4) Fluorite and fluorite-calcite veins in the Neoproterozoic Stuart Shelf successions were dated at 502 ± 14 Ma, which is consistent with the timing of the Delamerian Orogeny and an upgrading event in the Olympic Dam deposit. We postulate that fluorine-rich fluids remobilised metals from the fertile Olympic Province to the Neoproterozoic cover during the Delamerian Orogeny, which may have led to the development of sedimentary-hosted Cu-Co deposits such as those at Mount Gunson.
(5) Hence, the case studies illustrate the potential of the fluorite Lu-Hf method to reveal the timing of mineralisation and remobilisation, with significant implications for mineral exploration.

CRediT authorship contribution statement

Stijn Glorie: Conceptualization, Investigation, Methodology. **Jacob Mulder:** Resources, Investigation, Writing – review & editing. **Martin Hand:** Conceptualization. **Adrian Fabris:** Resources. **Alexander Simpson:** Methodology. **Sarah Gilbert:** Resources, Methodology.

Declaration of Competing Interest

The authors declare that they have no known competing financial interests or personal relationships that could have appeared to influence the work reported in this paper.

Acknowledgements

This paper was supported by research grants DP200101881 and FT210100906 from the Australian Research Council (ARC) and additionally by the Mineral Exploration Cooperative Research Centre. Carmen Krapf is thanked for assistance with drillcore access and suitable sample identification. Arthur Hickman is thanked for sampling advice in the Pilbara Craton. Jie Yu is thanked for assistance with sample preparation and analysis of the EDG-1 garnets. Kyle Larson and Kathryn Cutts are thanked for their helpful reviews.

Appendix A. Supplementary data

Supplementary data to this article can be found online at https://doi.org/10.1016/j.gsf.2023.101629.

References

Allen, S.R., McPhie, J., Ferris, G., Simpson, C., 2008. Evolution and architecture of a large felsic Igneous Province in western Laurentia: The 1.6 Ga Gawler Range Volcanics, South Australia. J. Volcanol. Geotherm. Res. 172, 132–147.
Apukhtina, O.B., Kamenetsky, V.S., Ehrig, K., Kamenetsky, M.B., Maas, R., Thompson, J., McPhie, J., Ciobanu, C.L., Cook, N.J., 2017. Early, deep magnetite-fluorapatite mineralization at the Olympic Dam Cu-U-Au-Ag deposit, South Australia. Econ. Geol. 112, 1531–1542.
Barker, S.L.L., Bennett, V.C., Cox, S.F., Norman, M.D., Gagan, M.K., 2009. Sm–Nd, Sr, C and O isotope systematics in hydrothermal calcite–fluorite veins: Implications for fluid–rock reaction and geochronology. Chem. Geol. 268, 58–66.
Bau, M., Romer, R.L., Lüders, V., Dulski, P., 2003. Tracing element sources of hydrothermal mineral deposits: REE and Y distribution and Sr-Nd-Pb isotopes in fluorite from MVT deposits in the Pennine Orefield. England. Mineral. Deposita 38, 992–1008.
Brown, D.A., Simpson, A., Hand, M., Morrissey, L.J., Gilbert, S., Tamblyn, R., Glorie, S., 2022. Laser-ablation Lu-Hf dating reveals Laurentian garnet in subducted rocks from southern Australia. Geology 50, 837–842.
Champion, D.C., Smithies, R.H., 2007. Geochemistry of Paleoarchean granites of the East Pilbara Terrane, Pilbara Craton, Western Australia: implications for early Archean crustal growth. In: Van Kranendonk, M.J., Bennett, V.C., Smithies, R.H. (Eds.), Earth's Oldest Rocks. Elsevier BV, Burlington, Massachusetts USA, pp. 369–410.
Cherniak, D.J., Zhang, X.Y., Wayne, N.K., Watson, E.B., 2001. Sr, Y, and REE diffusion in fluorite. Chem. Geol. 181, 99–111.
Cherry, A.R., Ehrig, K., Kamenetsky, V.S., McPhie, J., Crowley, J.L., Kamenetsky, M.B., 2018. Precise geochronological constraints on the origin, setting and incorporation of ca. 1.59 Ga surficial facies into the Olympic Dam Breccia Complex. South Australia. Precambrian Res. 315, 162–178.
Chesley, J.T., Halliday, A.N., Scrivener, R.C., 1991. Samarium-neodymium direct dating of fluorite mineralization. Science 252, 949–951.
Chew, D.M., Petrus, J.A., Kamber, B.S., 2014. U-Pb LA-ICPMS dating using accessory mineral standards with variable common Pb. Chem. Geol. 363, 185–199.
Ciobanu, C.L., Wade, B.P., Cook, N.J., Schmidt Mumm, A., Giles, D., 2013. Uranium-bearing hematite from the Olympic Dam Cu–U–Au deposit, South Australia: A geochemical tracer and reconnaissance Pb–Pb geochronometer. Precambrian Res. 238, 129–147.
Courtney-Davies, L., Ciobanu, C.L., Tapster, S.R., Cook, N.J., Ehrig, K., Crowley, J.L., Verdugo-Ihl, M.R., Wade, B.P., Condon, D.J., 2020. Opening the magmatic-hydrothermal window: high-precision U-Pb geochronology of the Mesoproterozoic Olympic Dam Cu-U-Au-Ag deposit, South Australia. Econ. Geol. 115, 1855–1870.
Duncan, R.J., Stein, H.J., Evans, K.A., Hitzman, M.W., Nelson, E.P., Kirwin, D.J., 2011. A new geochronological framework for mineralization and alteration in the Selwyn-Mount Dore Corridor, Eastern Fold Belt, Mount Isa Inlier, Australia: Genetic implications for iron oxide copper-gold deposits. Econ. Geol. 106, 169–192.
Ehrig, K., Kamenetsky, V.S., McPhie, J., Macmillan, E., Thompson, J., Kamenetsky, M., Maas, R., 2021. Staged formation of the supergiant Olympic Dam uranium deposit, Australia. Geology 49, 1312–1316.
Evans, N.J., Wilson, N.S.F., Cline, J.S., McInnes, B.I.A., Byrne, J., 2005. Fluorite (U–Th)/He thermochronology: Constraints on the low temperature history of Yucca Mountain. Nevada. Appl. Geochem. 20, 1099–1105.

Foden, J., Elburg, M.A., Dougherty-Page, J., Burtt, A., 2006. The timing and duration of the Delamerian Orogeny: Correlation with the Ross Orogen and implications for Gondwana assembly. J. Geol. 114, 189–210.
Foden, J., Elburg, M., Turner, S., Clark, C., Blades, M.L., Cox, G., Collins, A.S., Wolff, K., George, C., 2020. Cambro-Ordovician magmatism in the Delamerian orogeny: Implications for tectonic development of the southern Gondwanan margin. Gondwana Res. 81, 490–521.
Galindo, C., Tornos, F., Darbyshire, D.P.F., Casquet, C., 1994. The age and origin of the barite-fluorite (Pb□Zn) veins of the Sierra del Guadarrama (Spanish Central System, Spain): a radiogenic (Nd, Sr) and stable isotope study. Chem. Geol. 112, 351–364.
Gardiner, N.J., Hickman, A.H., Kirkland, C.L., Lu, Y.J., Johnson, T., Zhao, J.X., 2017. Processes of crust formation in the early Earth imaged through Hf isotopes from the East Pilbara Terrane. Precambrian Res. 297, 56–76.
Glorie, S., Gillespie, J., Simpson, A., Gilbert, S., Khudoley, A., Priyatkina, N., Hand, M., Kirkland, C.L., 2022. Detrital apatite Lu–Hf and U-Pb geochronology applied to the southwestern Siberian margin. Terra Nova 34, 201–209.
Glorie, S., Hand, M., Mulder, J., Simpson, A., Emo, R.B., Kamber, B.S., Fernie, N., Nixon, A., Gilbert, S., 2023. Robust laser ablation Lu-Hf dating of apatite: an empirical evaluation. Geological Society of London Special Publication, in press.
Groenlie, A., Roberts, D., Harder, V., 1990. Preliminary fission-track ages of fluorite mineralization along fracture zones, inner Trondheimsfjord, Central Norway. Norsk Geologisk Tidsskrift 70, 173–178.
Hand, M., Reid, A., Jagodzinski, L., 2007. Tectonic Framework and Evolution of the Gawler Craton, Southern Australia. Econ. Geol. 102, 1377–1395.
Hickman, A.H., 2021. East Pilbara Craton: a record of one billion years in the growth of Archean continental crust. Geological Survey of Western Australia Report 143, 187p.
Hickman, A.H., Van Kranendonk, M.J., 2012. Early Earth evolution: evidence from the 3.5-1.8 Ga geological history of the Pilbara region of Western Australia. Episodes 35, 283–297.
Huston, D.L., Sun, S.-S., Blewett, R., Hickman, A.H., Kranendonk, M.V., Phillips, D., Baker, D., Brauhart, C., 2002. The timing of mineralization in the Archean North Pilbara Terrain, Western Australia. Econ. Geol. 97, 733–755.
Jagodzinski, E.A., Reid, A.J., Crowley, J.L., Wade, C.E., Curtis, S., 2023. Precise zircon U-Pb dating of the Mesoproterozoic Gawler large igneous province, South Australia. Result. Geochem. 10, 100020.
Janousek, V., Farrow, C.M., Erban, V., 2006. Interpretation of whole-rock geochemical data in igneous geochemistry: Introducing Geochemical Data Toolkit (GCDkit). J. Petrol. 47, 1255–1259.
Johnson, J.P., Cross, K.C., 1995. U-Pb geochronological constraints on the genesis of the Olympic Dam Cu-U-Au-Ag deposit, South Australia. Econ. Geol. 90, 1046–1063.
Kendall, B., Creaser, R.A., Selby, D., 2006. Re-Os geochronology of postglacial black shales in Australia: Constraints on the timing of "Sturtian" glaciation. Geology 34, 729–732.
Kendall-Langley, L.A., Kemp, A.I.S., Grigson, J.L., Hammerli, J., 2020. U-Pb and reconnaissance Lu-Hf isotope analysis of cassiterite and columbite group minerals from Archean Li-Cs-Ta type pegmatites of Western Australia. Lithos 352 (353), 105231.
Kinny, P.D., 2000. U-Pb dating of rare metal (Sn-Ta-Li) mineralised pegmatites in Western Australia by SIMS analysis of tin and tantalum bearing ore minerals. New Frontiers in Isotope Geology Conference, Lorne, Victoria, pp. 113-116.
Knutson, J., Donnelly, T.H., Tonkin, D.G., 1983. Geochemical constraints on the genesis of copper mineralization in the Mount Gunson area, South Australia. Econ. Geol. 78, 250–274.
Lambert, I.B., Knutson, J., Donnelly, T.H., Etminan, H., 1987. Stuart Shelf-Adelaide Geosyncline copper province, South Australia. Econ. Geol. 82, 108–123.
Lenoir, L., Blaise, T., Somogyi, A., Brigaud, B., Barbarand, J., Boukari, C., Nouet, J., Brézard-Oudot, A., Pagel, M., 2021. Uranium incorporation in fluorite and exploration of U-Pb dating. Geochronology 3, 199–227.
Li, Y., Vermeesch, P., 2021. Short communication: Inverse isochron regression for Re–Os, K-Ca and other chronometers. Geochronology 3, 415–420.
Lloyd, J.C., Blades, M.L., Counts, J.W., Collins, A.S., Amos, K.J., Wade, B.P., Hall, J.W., Hore, S., Ball, A.L., Shahin, S., Drabsch, M., 2020. Neoproterozoic geochronology and provenance of the Adelaide Superbasin. Precambrian Res. 350, 105849.
Maas, R., Apukhtina, O.B., Kamenetsky, V.S., Ehrig, K., Sprung, P., Münker, C., 2022. Carbonates at the supergiant Olympic Dam Cu-U-Au-Ag deposit, South Australia part 2: Sm-Nd, Lu-Hf and Sr-Pb isotope constraints on the chronology of carbonate deposition. Ore Geol. Rev. 140, 103745.
Mao, M., Simandl, G.J., Spence, J., Marshall, D., 2015. Fluorite trace-element chemistry and its potential as an indicator mineral: Evaluation of LA-ICP-MS method. In: Simandl, G.J., Neetz, M., (Eds.), Symposium on Strategic and Critical Materials Proceedings, November 13-14, 2015, Victoria, British Columbia. British Columbia Ministry of Energy and Mines, British Columbia Geological Survey Paper 2015-3, pp. 251-264.
McPhie, J., Kamenetsky, V., Allen, S., Ehrig, K., Agangi, A., Bath, A., 2011. The fluorine link between a supergiant ore deposit and a silicic large igneous province. Geology 39, 1003–1006.
Möller, P., Parekh, P.P., Schneider, H.J., 1976. The application of Tb/Ca-Tb/La abundance ratios to problems of fluorspar genesis. Mineral. Deposita 11, 111–116.
Nebel, O., Morel, M.L.A., Vroon, P.Z., 2009. Isotope dilution determinations of Lu, Hf, Zr, Ta and W, and Hf isotope compositions of NIST SRM 610 and 612 Glass Wafers. Geostand. Geoanal. Res. 33, 487–499.
Nelson, D.R., 1998. 142879: biotite monzogranite, Cooglegong Creek; in Compilation of SHRIMP U-Pb zircon geochronology data. Western Australia Geological Survey Record 1998 (2), 157–159.
Nelson, D.R., 2004. 16944: muscovite-biotite monzogranite, Ripon Hills Road – Yandicoogina Creek crossing. Geochronolgoy dataset 130, Western Australia Geological Survey.
Nelson, D.R., 2005. 178014: biotite monzogranite, Quartz Hill. Geochronology dataset 551, Western Australia Geological Survey.
Norris, A., Danyushevsky, L., 2018. Towards Estimating the Complete Uncertainty Budget of Quantified Results Measured By LA-ICP-MS. Goldschmidt, Boston, USA.
Piccione, G., Rasbury, E.T., Elliott, B.A., Kyle, J.R., Jaret, S.J., Acerbo, A.S., Lanzirotti, A., Northrup, P., Wooton, K., Parrish, R.R., 2019. Vein fluorite U-Pb dating demonstrates post–6.2 Ma rare-earth element mobilization associated with Rio Grande rifting. Geosphere 15, 1958–1972.
Preiss, W.V., 1987. Adelaide geosyncline–late Proterozoic stratigraphy, sedimentation, palaeontology and tectonics. Geological Survey of South Australia Bulletin, Adelaide, South Australia, pp. 428.
Reid, A., 2019. The Olympic Cu-Au Province, Gawler Craton: A review of the lithospheric architecture, geodynamic setting, alteration systems, cover successions and prospectivity. Minerals 9 (6), 371.
Reid, A.J., Fabris, A., 2015. Influence of preexisting low metamorphic grade sedimentary successions on the distribution of iron oxide copper-gold mineralization in the Olympic Cu-Au Province, Gawler Craton. Econ. Geol. 110, 2147–2157.
Richardson, C.K., Holland, H.D., 1979. Fluorite deposition in hydrothermal systems. Geochim. Cosmochim. Acta 43, 1327–1335.
Roberts, N.M., Tikoff, B., 2021. Internal structure of the Paleoarchean Mt Edgar dome, Pilbara Craton, Western Australia. Precambrian Res. 358, 106163.
Sawyer, M., Whittaker, B., de Little, J., 2017. Carrapateena iron oxide Cu-Au-Ag-U deposit. In: Phillips, G.N., (Ed.), 2017 Australian Ore Deposits. The Australasian Institute of Mining and Metallurgy, Mono 32, pp. 615–620.
Schlegel, T.U., Wagner, T., Wälle, M., Heinrich, C.A., 2018. Hematite breccia-hosted iron oxide copper-gold deposits require magmatic fluid components exposed to atmospheric oxidation: Evidence from Prominent Hill, Gawler Craton, South Australia. Econ. Geol. 113, 597–644.
Schlegel, T.U., Wagner, T., Fusswinkel, T., 2020. Fluorite as indicator mineral in iron oxide-copper-gold systems: explaining the IOCG deposit diversity. Chem. Geol. 548, 119674.
Schmandt, D.S., Cook, N.J., Ciobanu, C.L., Ehrig, K., Wade, B.P., Gilbert, S., Kamenetsky, V.S., 2017. Rare Earth Element fluorocarbonate minerals from the Olympic Dam Cu-U-Au-Ag Deposit, South Australia. Minerals 7 (10), 202.
Schwinn, G., Markl, G., 2005. REE systematics in hydrothermal fluorite. Chem. Geol. 216, 225–248.
Simonetti, A., Heaman, L.M., Chacko, T., Banerjee, N.R., 2006. In situ petrographic thin section U-Pb dating of zircon, monazite, and titanite using laser ablation-MC-ICP-MS. Int. J. Mass Spectrom. 253, 87–97.
Simpson, A., Gilbert, S., Tamblyn, R., Hand, M., Spandler, C., Gillespie, J., Nixon, A., Glorie, S., 2021. In-situ Lu-Hf geochronology of garnet, apatite and xenotime by LA ICP MS/MS. Chem. Geol. 577, 120299.
Simpson, A., Glorie, S., Hand, M., Spandler, C., Gilbert, S., Cave, B., 2022. In situ Lu–Hf geochronology of calcite. Geochronology 4, 353–372.
Simpson, A., Hand, M., Glorie, S., Spandler, C., Gilbert, S., 2023. Garnet Lu-Hf speed dating: a novel method to rapidly resolve polymetamorphic histories. Gondwana Res. 121, 215–234.
Skirrow, R.G., Bastrakov, E.N., Baroncii, K., Fraser, G.L., Creaser, R.A., Fanning, C.M., Raymond, O.L., Davidson, G.J., 2007. Timing of iron oxide Cu-Au-(U) hydrothermal activity and Nd isotope constraints on metal sources in the Gawler craton, south Australia. Econ. Geol. 102, 1441–1470.
Spencer, C.J., Kirkland, C.L., Roberts, N.M.W., Evans, N.J., Liebmann, J., 2020. Strategies towards robust interpretations of in situ zircon Lu–Hf isotope analyses. Geosci. Front. 11, 843–853.
Sweetapple, M.T., Collins, P.L.F., 2002. Genetic Framework for the Classification and Distribution of Archean Rare Metal Pegmatites in the North Pilbara Craton, Western Australia. Econ. Geol. 97, 873–895.
Szpunar, M., Hand, M., Barovich, K., Jagodzinski, E., Belousova, E., 2011. Isotopic and geochemical constraints on the Paleoproterozoic Hutchison Group, southern Australia: Implications for Paleoproterozoic continental reconstructions. Precambrian Res. 187, 99–126.
Tamblyn, R., Hand, M., Simpson, A., Gilbert, S., Wade, B., Glorie, S., 2022. In situ laser ablation Lu–Hf geochronology of garnet across the Western Gneiss Region: campaign-style dating of metamorphism. J. Geol. Soc. 179, jgs2021-2094.
Tonkin, D., Wallace, C., 2021. Stratigraphy, diagenesis and copper sulfide mineralisation in the Whyalla Sandstone, Stuart Shelf, and implications for stratabound mineral exploration. MESA J. 94, 23–40.
Van Kranendonk, M.J., 2011. Cool greenstone drips and the role of partial convective overturn in Barberton greenstone belt evolution. J. Afr. Earth Sci. 60, 346–352.
Van Kranendonk, M.J., Hickman, A.H., Smithies, R.H., Champion, D.C., 2007. Paleoarchean development of a continental nucleus: the East Pilbara Terrane of the Pilbara Craton, Western Australia, In: Van Kranendonk, M.J., Bennett, V.C., Smithies, R.H. (Eds.), Earth's oldest rocks, Elsevier BV, Burlington, Massachusetts, USA, pp. 307–337.
Vermeesch, P., 2018. IsoplotR: A free and open toolbox for geochronology. Geosci. Front. 9, 1479–1493.

Wade, C.E., Payne, J.L., Barovich, K.M., Reid, A.J., Jagodzinski, E.A., Curtis, S., Hill, J., 2022. Temporal, geochemical and isotopic constraints on plume-driven felsic and mafic components in a Mesoproterozoic flood rhyolite province. Resul. Geochem. 9, 100019.

Wiemer, D., Schrank, C.E., Murphy, D.T., Wenham, L., Allen, C.M., 2018. Earth's oldest stable crust in the Pilbara Craton formed by cyclic gravitational overturns. Nat. Geosci. 11, 357–361.

Williams, M.R., Holwell, D.A., Lilly, R.M., Case, G.N.D., McDonald, I., 2015. Mineralogical and fluid characteristics of the fluorite-rich Monakoff and E1 Cu–Au deposits, Cloncurry region, Queensland, Australia: Implications for regional F-Ba-rich IOCG mineralisation. Ore Geol. Rev. 64, 103–127.

Williams-Jones, A.E., Samson, I.M., Olivo, G.R., 2000. The genesis of hydrothermal fluorite-REE deposits in the Gallinas Mountains, New Mexico. Econ. Geol. 95, 327–341.

Wingate, M.T.D., Kirkland, C.L., Hickman, A.H., 2015. 178011: biotite granodiorite, Cookes Creek. Geochronology Record 1226, Geological Survey of Western Australia, pp. 4.

Wolff, R., Dunkl, I., Kempe, U., von Eynatten, H., 2015. The age of the latest thermal overprint of tin and polymetallic deposits in the Erzgebirge, Germany: Constraints from fluorite (U-Th-Sm)/He thermochronology. Econ. Geol. 110, 2025–2040.

Wolff, R., Dunkl, I., Kempe, U., Stockli, D., Wiedenbeck, M., von Eynatten, H., 2016. Variable helium diffusion characteristics in fluorite. Geochim. Cosmochim. Acta 188, 21–34.

Xing, Y., Etschmann, B., Liu, W., Mei, Y., Shvarov, Y., Testemale, D., Tomkins, A., Brugger, J., 2019. The role of fluorine in hydrothermal mobilization and transportation of Fe, U and REE and the formation of IOCG deposits. Chem. Geol. 504, 158–176.